Green Chemistry

PAPER

View Article Online
View Journal | View Issue

Cite this: *Green Chem.*, 2026, **28**, 7506

Defect-engineered Cu_2O/Co_xO heterostructures with built-in electric fields for high-current-density alkaline water splitting

Tingting Tang,[a] Zhendong Gao,[a] Kuoteng Sun,[c] Chenggong Niu,[a] Chenxi Shang,[a] Jingya Guo,[a] Jianniao Tian, *[a] Tayirjan Taylor Isimjan*[b] and Xiulin Yang *[a]

Received 22nd December 2025,
Accepted 31st March 2026

DOI: 10.1039/d5gc06935a

rsc.li/greenchem

Developing cost-effective, high-performance electrocatalysts for the oxygen evolution reaction (OER) is critical to advancing alkaline water electrolysis and renewable hydrogen production. Here, we report a heterostructured Cu_2O/Co_xO catalyst grown on nickel foam (Cu_2O/Co_xO@NF), constructed *via* phytic acid etching and $NaBH_4$-mediated reduction, which optimizes structural, electronic, and interfacial properties. The catalyst exhibits a high specific surface area of 91.76 $m^2\ g^{-1}$, abundant Cu-derived defect sites, and a built-in electric field (BIEF) from the Cu_2O–Co_xO work function difference ($\Delta\Phi$ = 0.13 eV). These features enhance charge separation, *OH adsorption, and the formation of active CoOOH/CuOOH phases. Cu_2O/Co_xO@NF achieves exceptionally low overpotentials of 194, 298, and 333 mV at 10, 100, and 200 mA cm^{-2}, outperforming Co_xO@NF, Cu_2O@NF, and commercial RuO_2. It further delivers the highest double-layer capacitance (C_{dl} = 296.2 mF cm^{-2}), the lowest charge-transfer resistance, and early onset of CoOOH formation (1.40 V *vs.* RHE). *In situ* FTIR identifies a strong *OOH signal at ~1130 cm^{-1}, confirming accelerated OER kinetics. During long-term testing, the catalyst maintains stable operation for 450 h at 100 mA cm^{-2}. In a two-electrode electrolyzer, Cu_2O/Co_xO@$NF^{(+)}$||Pt/C@$NF^{(-)}$ requires only 1.77, 1.86, 1.94, and 2.01 V to reach 100–400 mA cm^{-2}, surpassing RuO_2@NF benchmarks. The catalyst also demonstrates a high faradaic efficiency of 98.57% and exceptional operational durability over 560 h. Finally, water splitting driven by a solar cell and a wind-powered battery demonstrates practical applicability for decentralized hydrogen production.

Green foundation

1. To advance sustainable hydrogen production, this work reports a heterostructured Cu_2O/Co_xO catalyst using Earth-abundant metals as a green substitute for expensive RuO_2. It achieves superior efficiency through reduced overpotential and enhanced durability, thereby lowering both economic and environmental costs.
2. The catalyst exhibits benchmark performance, achieving an ultralow overpotential of 194 mV at 10 mA cm^{-2} (outperforming commercial RuO_2), a full-cell voltage of 1.77 V at 100 mA cm^{-2}, >450 h stability under industrial current density, and a faradaic efficiency of 98.57% for efficient hydrogen production.
3. The current synthesis utilizes $NaBH_4$ and phytic acid, indicating potential for optimization with greener alternatives. Future work should include a systematic life cycle assessment to evaluate industrial-scale environmental impact and recyclability, as well as a full assessment of the sustainability of alkaline electrolyte use.

1. Introduction

The oxygen evolution reaction (OER), a kinetically sluggish four-electron transfer process under alkaline conditions, is the rate-determining step in water electrolysis—a core technology for green hydrogen production.[1–3] Two major bottlenecks constrain OER performance: the interfacial properties between the electrode and the electrolyte and the charge-transfer efficiency within the electrode material.[4,5] Electrode hydrophilicity directly governs electrolyte spreading and infiltration.[6,7] At the same time, efficient charge transfer depends on ordered internal charge-transport channels, in which a built-in electric field (BIEF) can regulate charge distribution, lower reaction energy barriers, and accelerate electron/ion transport.[8,9] Although cobalt- and copper-based oxides have been widely studied for their intrinsic catalytic activity and cost advantages,

[a]*Guangxi Key Laboratory of Low Carbon Energy Materials, School of Chemistry and Pharmaceutical Sciences, Guangxi Normal University, Guilin 541004, China. E-mail: xlyang@gxnu.edu.cn, birdtjn@sina.com*
[b]*Saudi Arabia Basic Industries Corporation (SABIC) at King Abdullah University of Science and Technology (KAUST), Thuwal 23955-6900, Saudi Arabia. E-mail: isimjant@sabic.com*
[c]*Liuzhou Bureau of EHV Transmission Company of China Southern Power Grid Co. Ltd, Liuzhou 545006, China*

they typically suffer from two fundamental limitations: (i) insufficient intrinsic hydrophilicity, which restricts effective contact between the electrolyte and active sites, and (ii) low charge-transfer efficiency, which results in sluggish reaction kinetics.[10–12] Single approaches, such as structural modification or elemental doping, are unable to address both issues simultaneously, underscoring the urgent need for innovative electrode material designs.

Recent efforts have attempted to enhance catalyst performance through strategies such as nanostructure engineering and defect engineering. Flower-like microstructures—with high specific surface areas, abundant porosity, and open reaction sites—not only enlarge the contact area between the electrode and the electrolyte but also shorten ion-transport pathways.[13,14] Defect engineering, a powerful means to modulate surface reactivity, enhances reactant adsorption and generates additional active sites.[15,16] Moreover, the introduction of metal defects induces a non-uniform charge distribution, potentially creating built-in electric fields that accelerate charge separation and transport, thereby improving catalytic kinetics.[17–19] However, most existing studies remain limited to single-strategy optimization, making it difficult to simultaneously enhance mass transport at the electrode/electrolyte interface and charge transport within the material.[20,21] Therefore, integrating optimized macroscopic wettability with tailored microscopic electronic structures—thus overcoming the dual bottlenecks of hydrophilicity and charge transport—represents a key scientific question and a significant challenge in this field.

Our strategy synergistically integrates structural and electronic engineering. The 3D nanoflower architecture and superhydrophilic surface maximize active-site exposure and enable efficient mass transport. At the same time, the BIEF and Cu-induced defects collaboratively optimize charge separation and guide the formation of the active phase. Specifically, the flower-like composite oxide provides abundant channels for electrolyte penetration, markedly reducing the interfacial contact angle. Simultaneously, metal defects within the Co/Cu lattice induce directional electron migration, and the constructed BIEF accelerates charge separation and transfer while optimizing the OER energy barrier landscape.

To contextualize our work within the OER catalyst landscape, we compare the design philosophy of Cu_2O/Co_xO with state-of-the-art Co–Cu systems (Table S1). While previous studies have typically addressed charge-transfer enhancement (*e.g.*, through heterojunction engineering) and active-site optimization (*e.g.*, *via* geometric modulation or defect introduction) as separate objectives, our approach integrates both into a unified and synergistic framework.

The Cu_2O/Co_xO heterojunction establishes a strong BIEF that functions as a "directed highway" for hole transport, while the intentionally introduced Cu vacancies at the interface serve as optimized "traffic hubs" for OER intermediates. This field-assisted defect catalysis enables an exceptional balance between activity and stability—effectively overcoming the common trade-off observed in defect-rich catalysts—and proposes a broadly applicable design principle for next-generation electrocatalysts.

This combined structural and electronic regulation endows the material with both high catalytic activity and excellent long-term cycling stability, effectively overcoming the long-standing trade-off between activity and stability in conventional electrode materials. The primary objectives of this study are to systematically evaluate the OER performance of the synthesized Co/Cu composite oxide—targeting a low overpotential at 100 mA cm^{-2} and strong operational stability—and to demonstrate its practical applicability in an alkaline water electrolyzer benchmarked against the commercial $RuO_2\|Pt/C$ catalyst. This comprehensive approach yields a high-performance catalyst that advances the development of efficient electrodes for practical water splitting, contributing to the realization of low-energy, large-scale green hydrogen production and the construction of a next-generation energy system.

2. Experimental section

2.1 Materials

Cobalt nitrate hexahydrate ($Co(NO_3)_2{\cdot}6H_2O$, 99.0%, Aladdin), copper(II) nitrate trihydrate ($Cu(NO_3)_2{\cdot}3H_2O$, 99%, Aladdin), urea ($CO(NH_2)_2$, 99.0%, Aladdin), ammonium fluoride (NH_4F, 96.0%, Aladdin), phytic acid solution (PA, 70.0% in H_2O, Aladdin), sodium borohydride ($NaBH_4$, ≥98.0%, Xilong Scientific), sodium hydroxide (NaOH, 96.0%, Aladdin), ethanol (C_2H_5OH, 99.7%, Xilong), Nafion (5 wt%, Alfa Aesar), Pt/C (20 wt% Pt, Sinero), and nickel foam (NF) used as a substrate (thickness of 1.6 mm, Suzhou Sinero Technology Co, Ltd) were obtained commercially. RuO_2 powder was prepared by directly annealing $RuCl_3{\cdot}3H_2O$ (37%, Inno-Chem) at 400 °C in air. Deionized water (18.2 MΩ cm^{-2}) was produced using an ultrapure water system (Millipore). All starting materials and reagents were purchased from commercial suppliers and utilized directly.

2.2 Nickel foam (NF) pretreatment

Nickel foam (NF) was cut into pieces measuring 1.5 cm × 3.0 cm, followed by sequential ultrasonic cleaning in 3 M HCl (20 min), acetone (15 min), and ethanol (15 min) to remove surface oxides and organic contaminants. After each cleaning step, the samples were thoroughly rinsed with deionized water and subsequently dried in a vacuum oven at 60 °C for 6 h.

2.3 Synthesis of $CoCuHO/Co_3O_4$

For precursor preparation, 1.25 mmol of $Co(NO_3)_2{\cdot}6H_2O$, 0.6 mmol of $Cu(NO_3)_2{\cdot}6H_2O$, 2.0 mmol of NH_4F, and 2.5 mmol of $CO(NH_2)_2$ were dissolved in 40 mL of deionized water under magnetic stirring for 30 min to obtain a homogeneous solution. The pretreated NF was then immersed in the solution and transferred into a 100 mL Teflon-lined stainless-steel autoclave. The autoclave was sealed and heated in

an electric oven to 140 °C at a ramping rate of approximately 3 °C min^{-1}, and maintained at this temperature for 8 h. After the reaction, the autoclave was allowed to cool naturally to room temperature (~25 °C) before opening. The obtained product was collected, thoroughly washed with deionized water and ethanol, and dried at 60 °C for 3 h, yielding the $CoCuHO/Co_3O_4$ catalyst.

2.4 Synthesis of CuO/Co_3O_4

The $CoCuHO/Co_3O_4$ precursor was placed in a tube furnace and subjected to annealing at 400 °C for 180 min with a heating rate of 5 °C min^{-1} under an N_2 atmosphere, yielding the final CuO/Co_3O_4 product.

2.5 Synthesis of Cu_2O/Co_3O_4

A 0.1 M phytic acid (PA) solution was prepared by diluting 0.65 mL of a 50 wt% PA stock solution with 30 mL of deionized water. Subsequently, 10 mL of this PA solution was mixed with 10 mL of absolute ethanol in a 100 mL beaker to prepare the etching solution. The as-synthesized CuO/Co_3O_4 material was fully immersed in the mixed solution and allowed to etch at room temperature (25 ± 2 °C) for 5 h. After completion of the reaction, the solid product was washed sequentially three times with deionized water and twice with ethanol to remove residual PA and by-products, and then dried in air at 60 °C for 3 h, yielding the intermediate Cu_2O/Co_3O_4 catalyst.

2.6 Synthesis of Cu_2O/Co_xO

The as-prepared Cu_2O/Co_3O_4 intermediate was subjected to chemical reduction as follows: a sodium borohydride ($NaBH_4$) solution was freshly prepared by dissolving 0.1 g of $NaBH_4$ powder in 20 mL of ice-cold deionized water under gentle stirring to minimize premature hydrolysis. The intermediate was fully immersed in this solution, and the reduction was carried out under continuous magnetic stirring at room temperature (25 ± 2 °C) for 10 h. After completion of the reaction, the product was washed sequentially three times with deionized water and twice with absolute ethanol to remove residual reagents and by-products, and finally vacuum-dried at 60 °C for 6 h to obtain the final C_2O/Co_xO catalyst.

Similarly, the individual components, Cu_2O and Co_xO, were synthesized by following the same method as that for the Cu_2O/Co_xO composite.

2.7 Synthesis of RuO_2/NF and 20 wt% Pt/C/NF electrodes

Commercial $RuCl_3 \cdot 3H_2O$ was converted to RuO_2 *via* standard calcination in air at 400 °C for 3 h. A catalyst ink was then prepared by ultrasonically dispersing 2 mg of the as-prepared RuO_2 along with 20 wt% Pt/C in a mixture of 200 μL deionized water, 200 μL ethanol, and 10 μL of 5 wt% Nafion solution for 30 min. This homogeneous suspension was subsequently drop-cast onto clean nickel foam (NF, 1 × 1 cm^2) and allowed to dry under ambient conditions.

3. Results and discussion

3.1. Characteristics and structure of Cu_2O/Co_xO@NF catalysts

The schematic synthesis process of the Cu_2O/Co_xO@NF heterostructured catalysts is shown in Fig. 1a. After hydrothermal treatment, numerous nanoflower-like precursors (denoted as $CoCuHO/Co_3O_4$@NF) were uniformly grown on the NF surface (Fig. 1c-1 and Fig. S2a). Subsequent heat treatment under a nitrogen atmosphere preserved this distinctive morphology without noticeable structural changes (Fig. 1c-2 and Fig. S2b). Further etching with phytic acid followed by reduction with sodium borohydride induced a phase transformation from Cu_2O/Co_3O_4@NF (Fig. 1c-3 and Fig. S2c) to the final Cu_2O/Co_xO@NF. As shown in Fig. 1b, the XRD pattern confirms the presence of CoO (JCPDS 75-0418), Co_3O_4 (JCPDS 74-2120), and Cu_2O (JCPDS 74-1230), consistent with the formation of the intended heterostructure. The reference samples, Co_xO@NF and Cu_2O@NF, display single-phase structures (Fig. S3). Throughout the reaction sequence, the final catalyst retains its nanoflower-like morphology. The TEM image (Fig. 1e) reveals that the catalyst consists of interconnected nanosheets assembled into a flower-like architecture.

The high-resolution TEM (HRTEM) image (Fig. 1f) clearly shows the coexistence of Cu_2O, CoO, and Co_3O_4 crystalline domains. Well-defined lattice fringes with spacings of 0.300 nm (Cu_2O (110)), 0.213 nm (Cu_2O (200)), 0.212 nm (CoO (200)), 0.245 nm (Co_3O_4 (311)), and 0.285 nm (Co_3O_4 (220)) are observed (Fig. 1g). The corresponding selected-area electron diffraction (SAED) pattern (Fig. 1h) further confirms the polycrystalline nature of the composite. Moreover, elemental mapping obtained by high-angle annular dark-field scanning TEM (HAADF-STEM) and energy-dispersive X-ray spectroscopy (EDX) (Fig. 1i–k) shows a uniform distribution of Co, Cu, and O throughout the structure, conclusively verifying both the heterostructure and the catalyst's composition.

The porous structures of the catalysts were characterized by N_2 physisorption. All samples exhibit type III isotherms with mesoporous characteristics, as further confirmed by their pore-size distributions (Fig. 2a and b). Among them, the Cu_2O/Co_xO@NF composite shows the highest specific surface area (91.76 m^2 g^{-1}), accompanied by a pore volume of 12.73 cm^3 g^{-1}. Compared with Co_xO@NF (79.83 m^2 g^{-1}, 7.14 cm^3 g^{-1}) and Cu_2O@NF (36.60 m^2 g^{-1}, 8.26 cm^3 g^{-1}), these results indicate that the hierarchical nanoflower architecture does not merely increase porosity but instead creates a finely tuned mesoporous network. This optimized structure provides an ideal platform for improved mass and electron transport, thereby enhancing catalytic activity.[22] The structural refinement can be primarily attributed to the phytic acid etching step, which significantly increases the specific surface area (Fig. S4). Electron paramagnetic resonance (EPR) spectroscopy was used to probe the types and concentrations of defects in the catalysts. No significant EPR signals were observed for the $CoCuHO/Co_3O_4$@NF and CuO/Co_3O_4@NF precursors. In contrast, after phytic acid treatment, the Cu_2O/Co_3O_4@NF sample

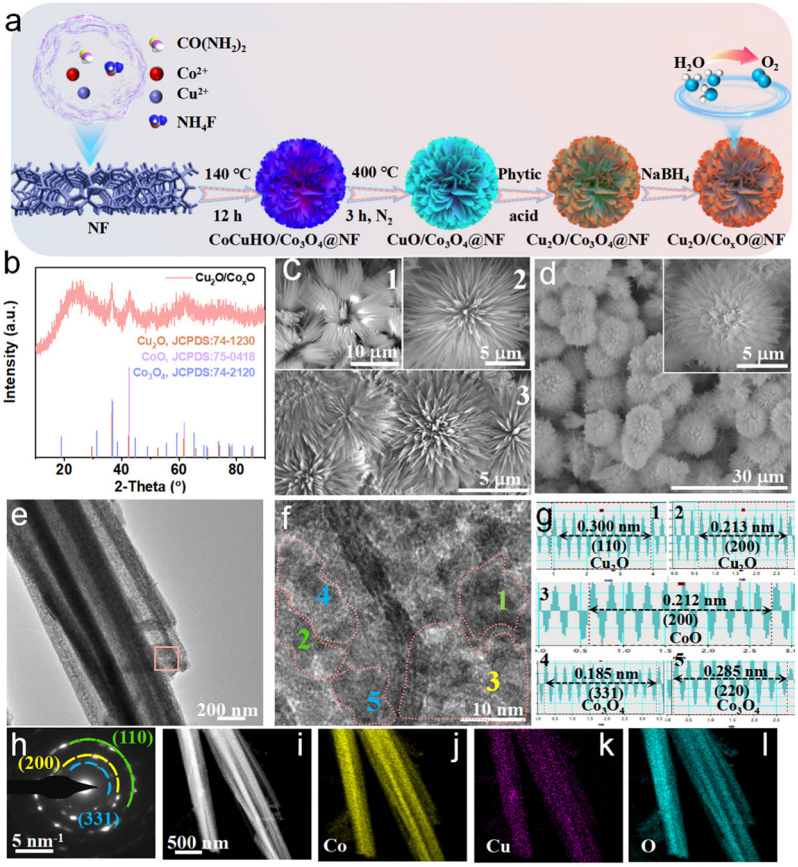

Fig. 1 (a) Synthesis route for Cu_2O/Co_xO@NF composites. (b) XRD pattern of Cu_2O/Co_xO_y@NF. SEM images of (c-1) CoCuHO/Co_3O_4@NF, (c-2) CuO/Co_3O_4@NF, (c-3) Cu_2O/Co_3O_4@NF, and (d) Cu_2O/Co_xO@NF. (e) TEM image, (f) high-resolution TEM (HRTEM) image, and (g) the corresponding intensity profile obtained from the HRTEM image of Cu_2O/Co_xO@NF. (h) SAED pattern, (i) HAADF-STEM image, and (j–l) the corresponding elemental maps: (j) Co, (k) Cu, and (l) O of Cu_2O/Co_xO@NF.

exhibited a distinct signal at g = 2.30 (Fig. S5), attributable to metallic vacancies formed through the complexation and extraction of metal ions by phytic acid. Subsequent reduction with $NaBH_4$—yielding the final Cu_2O/Co_xO@NF catalyst—produced a symmetric and markedly stronger signal at g = 2.16. This enhancement reflects a substantially higher defect density, arising from the reduction of surface metal ions and the accompanying lattice reconstruction, which together generate and stabilize metal vacancies.[23]

Comparison with the control samples (Fig. 2c) confirms the nature of these defects: Co_xO@NF shows no detectable signal, and Cu_2O@NF displays only a weak feature at g = 2.47. In contrast, the prominent signal in Cu_2O/Co_xO@NF corresponds to copper vacancies.[24] The presence of these moderate Cu defects is crucial, as they facilitate electron transfer and accelerate reaction kinetics.[25] Zeta potential (ζ) measurements in KOH solution reveal that Cu_2O/Co_xO@NF possesses a more negative surface charge (−25.3 mV) compared to Co_xO@NF (−19.2 mV) and Cu_2O@NF (−13.7 mV) (Fig. 2d). This increased surface negativity implies a higher density of adsorbed OH^- within the inner Helmholtz layer, promoting efficient charge accumulation and thereby enhancing OER activity in alkaline media.[26] These results highlight the importance of surface charge engineering for catalytic optimization.[27] Contact-angle measurements confirm that Cu_2O/Co_xO@NF exhibits strong hydrophilicity (28.2°, Fig. 2e), in sharp contrast to the hydrophobic Co_xO@NF (101.6°) and Cu_2O@NF (121.4°). This pronounced hydrophilicity enhances catalytic performance through three interconnected mechanisms: (i) it enables thorough electrolyte penetration, maximizing active-site accessibility and electrochemical surface area (supported by the high C_{dl}, Fig. 4d);[7] (ii) it reduces gas-bubble adhesion, facilitating rapid O_2 release and improving operational stability under high current densities (Fig. 4f);[28] and (iii) it optimizes the electrode–electrolyte interface, lowering charge-transfer resistance (Fig. S15) and overpotential.[6] Collectively, these effects contribute significantly to the superior activity and durability of the catalyst.[29] Cyclic voltammetry (CV) curves show a negative shift in the oxidation peak potential for the Cu_2O/Co_xO@NF electrode relative to the control samples (Fig. 2f). This shift reflects a redistribution of interfacial electrons within the heterostructure, enhancing interactions with hydroxyl species (*OH).[27] The resulting optimized *OH adsorption effectively lowers the energy barrier for the initial OER step, thereby accelerating surface reaction kinetics.[30]

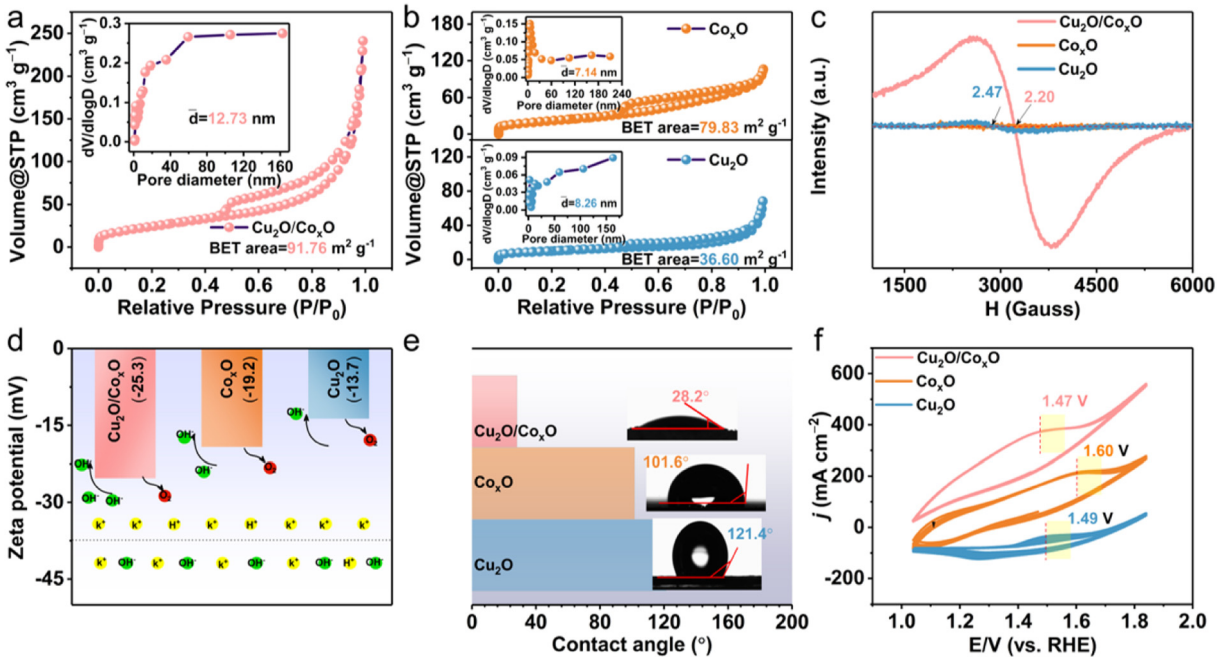

Fig. 2 N_2 adsorption–desorption isotherms of (a) Cu_2O/Co_xO@NF and (b) Co_xO@NF + Cu_2O@NF; the corresponding pore-size distribution curves are shown in the insets. (c) Electron paramagnetic resonance (EPR) spectra, (d) zeta potential in 1.0 M KOH, (e) contact angles with a 1.0 M KOH droplet, and (f) an enlarged view of the Co^{2+}/Co^{3+} redox peaks from CV curves in 1.0 M KOH at 5 mV s^{-1} of Cu_2O/Co_xO@NF, Co_xO@NF, and Cu_2O@NF, respectively.

X-ray photoelectron spectroscopy (XPS) was employed to investigate the elemental composition and chemical states of the Cu_2O/Co_xO@NF composite. The survey spectrum (Fig. S6a) confirms the presence of Co, Cu, and O, with the C 1s peak at 284.8 eV used for binding-energy calibration (Fig. S6b). In the high-resolution Co 2p spectrum (Fig. 3a), the deconvoluted peaks reveal the coexistence of Co^{2+} and Co^{3+} species. The spin–orbit doublets at 781.36/796.92 eV and their satellite peaks (785.58/802.50 eV) correspond to Co^{2+}, while the doublets at 779.46/795.79 eV are assigned to Co^{3+}.[31,32] Notably, the Co^{3+}/Co^{2+} ratio in Cu_2O/Co_xO@NF (0.98) is markedly lower than that in Co_xO@NF (2.33), demonstrating heterostructure-induced Co^{2+} enrichment. The abundance of low-valence Co^{2+} is crucial, as it readily undergoes pre-oxidation to form highly active Co^{3+}/Co^{4+} species during the OER, while simultaneously promoting the formation of an amorphous active layer. This synergistic combination of increased active-site density and facilitated charge transfer collectively accelerates the reaction kinetics.[33,34] The Cu 2p XPS spectrum of Cu_2O/Co_xO@NF (Fig. 3b) exhibits characteristic spin–orbit doublets (Cu $2p_{3/2}$ and Cu $2p_{1/2}$). Deconvolution reveals two oxidation states: peaks at 932.41 and 952.31 eV correspond to Cu^+, while peaks at 934.10 and 954.67 eV are assigned to Cu^{2+}. Quantitative analysis shows a higher proportion of Cu^+ than in Cu_2O@NF, indicating heterostructure-induced Cu^+ enrichment.[10,35] We propose that these abundant Cu^+ species act as electron donors and are pre-oxidized *in situ* to generate active Cu^{2+}/Cu^{3+} sites, while concurrently modulating adjacent cobalt centers to promote Co^{4+} formation. This interfacial synergy facilitates the development of a highly active reconstructed surface, thereby accelerating OER kinetics.[36] The high-resolution O 1s spectrum (Fig. 3c) presents three distinct peaks at 529.48, 530.86, and 531.71 eV, corresponding to metal–oxygen (M–O), metal–hydroxyl (M–OH), and adsorbed water species (H_2O_{ads}), respectively.[37]

To further elucidate the electronic structure and interfacial charge-transfer behavior, ultraviolet photoelectron spectroscopy (UPS) and UV-Vis diffuse reflectance spectroscopy were conducted. The UPS-derived valence band maximum (VBM) of Cu_2O/Co_xO@NF is located 1.03 eV below the Fermi level (Fig. 3d), which is deeper than those of Cu_2O@NF (1.75 eV) and Co_xO@NF (1.45 eV). This deeper VBM indicates an upward shift in the band structure, which is more favorable for surface oxidation reactions.[38] Furthermore, the measured work functions (Φ) of Cu_2O@NF and Co_xO@NF are 6.19 eV and 6.32 eV, respectively (Fig. 3d). This difference ($\Delta\Phi$ = 0.13 eV) induces spontaneous electron transfer from Cu_2O to Co_xO upon contact, establishing a built-in electric field (BEF) at the heterointerface.[8] Bandgap (E_g) values derived from the Tauc plots (Fig. 3e) were used to construct the energy-band diagram shown in Fig. 3f, providing insight into the charge-separation mechanism within the NF/Cu_xO/Cu_2O composite. The diagram reveals two distinct work functions (E_f = 6.32 eV for NF and E_f = 6.19 eV for the Cu_xO/Cu_2O heterojunction), which give rise to a built-in electric field (BIEF) directed from Cu_2O toward Co_xO. Upon illumination, photogenerated electrons in Cu_2O are driven by this BIEF, migrating from the conduction band minimum of Cu_2O (E_{CBM} = −6.24 eV) across the interface

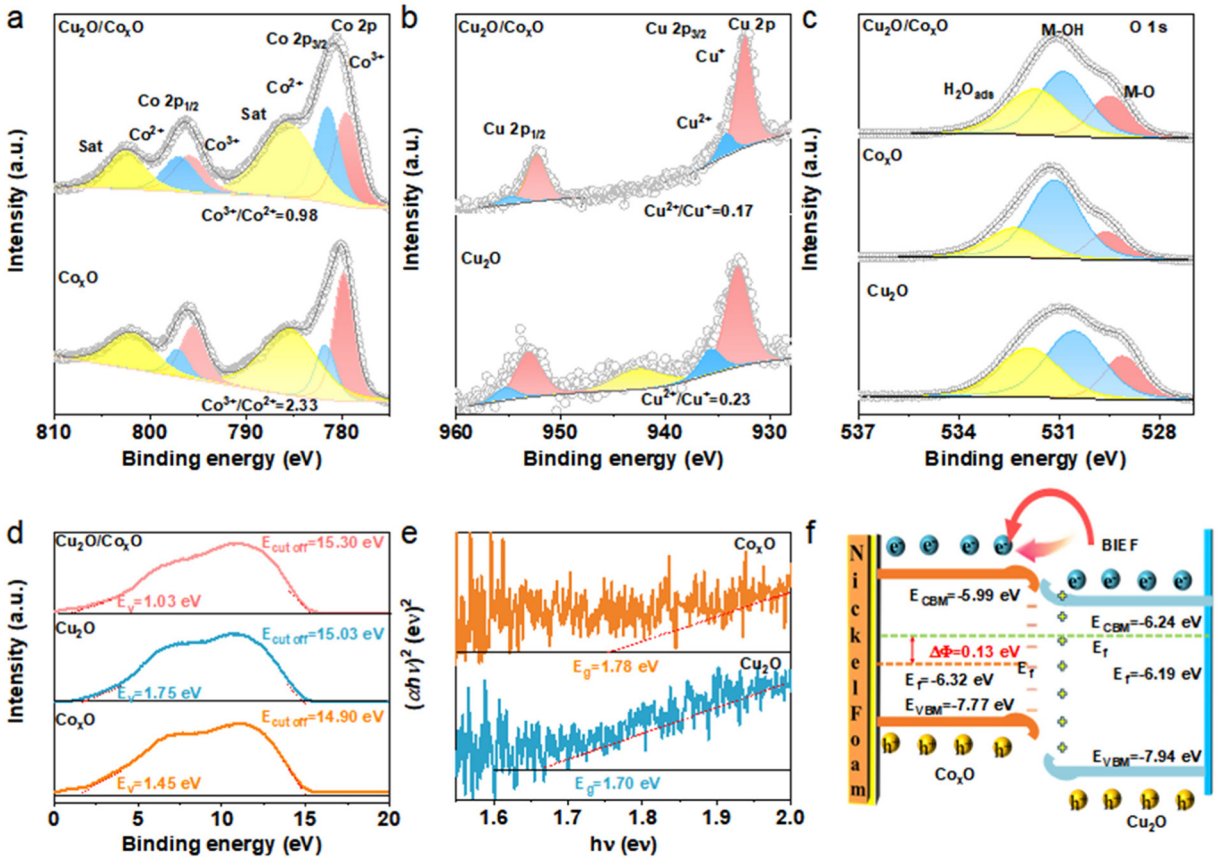

Fig. 3 High resolution XPS spectra of (a) Co 2p, (b) Cu 2p, and (c) O 1s of the designed catalysts. (d) UPS spectra. (e) UV/Vis spectra and (f) the corresponding energy band diagrams of Co_xO@NF and Cu_2O@NF.

to the conduction band of Co_xO (E_{CBM} = −5.99 eV). This directional electron transfer effectively suppresses charge-carrier recombination and promotes efficient charge separation, thereby accelerating reaction kinetics and enhancing the overall catalytic performance.[9,39]

The BIEF at the Cu_2O/Co_xO interface is supported by the UPS-derived work-function difference ($\Delta\Phi$ = 0.13 eV) and the significantly reduced charge-transfer resistance (R_{ct}) observed in EIS measurements. This $\Delta\Phi$ value is consistent with reported data for BIEF-confirmed Co/Cu-based heterojunctions,[40–42] reinforcing the plausibility of interfacial field formation. The enhanced OER activity and kinetics are attributed to BIEF-driven interfacial charge redistribution, which optimizes surface electron density and modulates intermediate adsorption. Direct quantitative determination of the BIEF strength and its correlation with OER performance will be explored in future studies using techniques such as Mott–Schottky analysis and Kelvin probe force microscopy.

3.2. OER performance

The OER performance of the synthesized catalysts was evaluated in 1.0 M KOH using a standard three-electrode system. The synthesis conditions for the Cu_2O/Co_xO@NF precursor catalyst were systematically optimized by varying the phytic acid soaking time and hydrothermal temperature (Fig. S11–S14). All electrochemical data were processed according to standard electrocatalysis *iR* compensation protocols.[43] High-frequency resistance (R_{HFR}) from EIS fitting (SI) was used for *iR* correction, with 85% compensation (a field-accepted practice) applied to avoid potentiostat oscillation and overcompensation.[44] Uncompensated and 85% *iR*-corrected LSV curves are plotted side by side (Fig. S16 and S17), eliminating artificial overpotential underestimation and ensuring reliable OER performance evaluation. Among the variants, the sample treated with phytic acid for 5 h exhibited the best activity, significantly outperforming Cu_2O@NF, Co_xO@NF, and even commercial RuO_2 (Fig. 4a). This optimized catalyst required overpotentials of only 194, 298, and 333 mV to reach current densities of 10, 100, and 200 mA cm^{-2}, respectively (Fig. 4b). To decouple the catalytic contribution from the nickel foam substrate, a control catalyst was synthesized on carbon paper (Cu_2O/Co_xO@CC) under identical conditions. This Cu_2O/Co_xO@CC electrode exhibited slightly inferior performance compared to its NF-supported counterpart (Fig. S7), confirming that the superior activity of Cu_2O/Co_xO@NF originates from the intrinsic catalytic properties of the material. SEM analysis (Fig. S8) revealed that the CC-supported catalyst formed blocky structures, whereas Cu_2O/Co_xO@NF maintained a nanoflower morphology, providing a substantially higher active surface area.

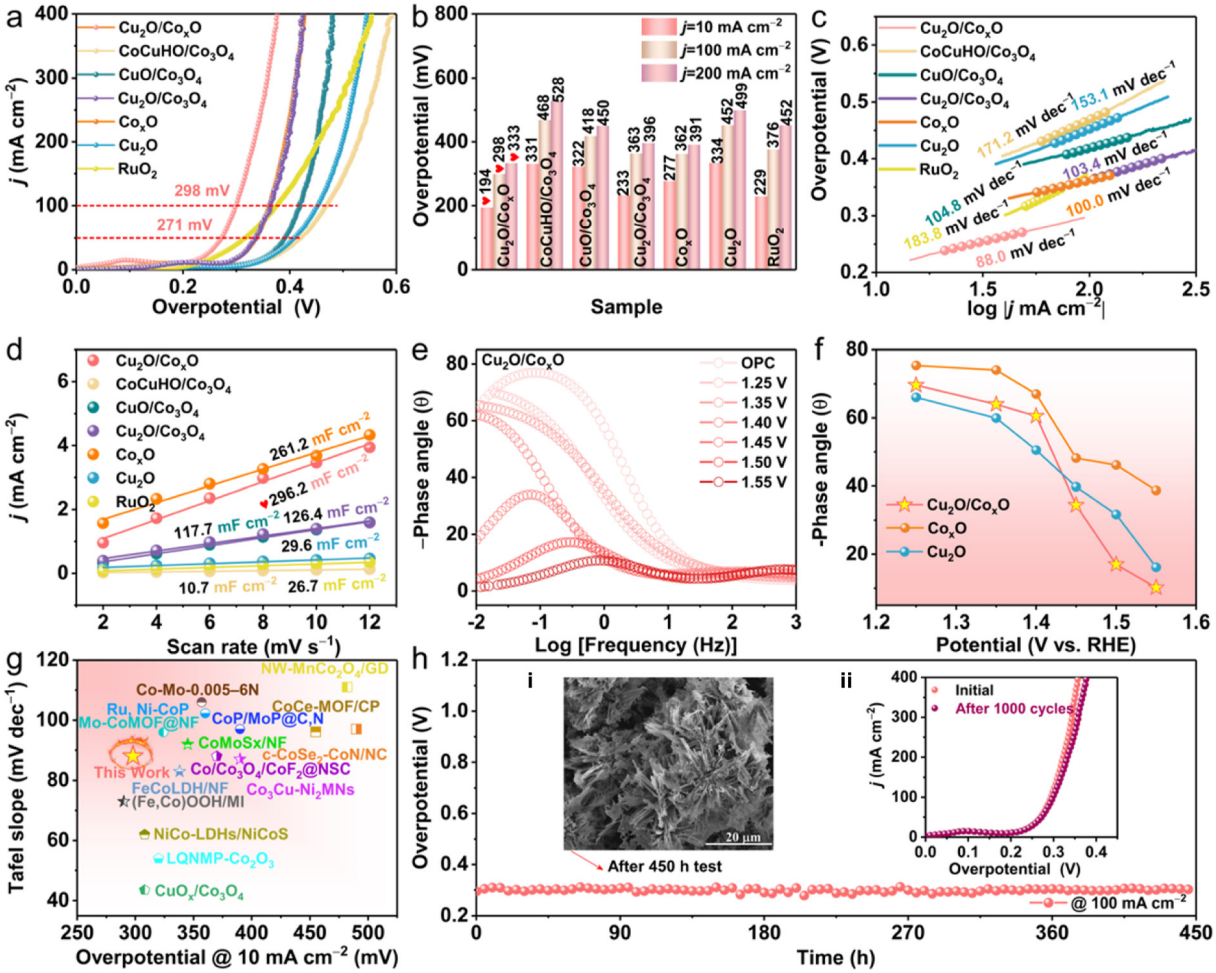

Fig. 4 OER performance of various samples measured in 1 M KOH. (a) Polarization curves. All potentials are *iR*-corrected. (b) Overpotentials at different current densities. (c) Tafel slopes. (d) C_{dl}. (e) Bode phase plots of Cu_2O/Co_xO@NF. (f) Response of the phase angle to the applied potential for different catalysts. (g) Comparison of η@100 mA cm^{-2} and Tafel slopes with benchmark OER catalysts. (h) Stability evaluation of Cu_2O/Co_xO@NF at a static overpotential of 100 mV. Insets: (i) SEM image of the electrode after operation at 100 mA cm^{-2}; (ii) polarization curves obtained before and after 1000 CV cycles. All potentials are *iR*-corrected.

Tafel slope analysis (Fig. 4c) shows that Cu_2O/Co_xO@NF exhibits the lowest slope (88.0 mV dec^{-1}) among all investigated catalysts, surpassing $CoCuHO/Co_3O_4$@NF (171.2 mV dec^{-1}), CuO/Co_3O_4@NF (104.8 mV dec^{-1}), Cu_2O/Co_3O_4@NF (103.4 mV dec^{-1}), Co_xO@NF (100.0 mV dec^{-1}), Cu_2O@NF (153.1 mV dec^{-1}), and RuO_2@NF (183.8 mV dec^{-1}). This enhanced kinetic performance is attributed to the synergistic interaction between Co_xO and Cu_2O, which increases charge-transfer efficiency.[45] The reduced Tafel slope of the target catalyst suggests a modification of the rate-determining step, which can be attributed to the interfacial built-in electric field optimizing the adsorption energy of oxygen evolution intermediates at the heterointerface. The electrochemically active surface area (ECSA), estimated from double-layer capacitance (C_{dl}) in the non-faradaic region (Fig. S10), provides further insight into the catalyst's performance.[46] As shown in Fig. 4d, Cu_2O/Co_xO@NF exhibits a C_{dl} of 296.2 mF cm^{-2}, the highest among all samples, and the corresponding ECSA follows the same trend. These results confirm that the Co_xO-Cu_2O synergy maximizes the exposure of active sites and promotes efficient reaction processes. To distinguish the contribution of active-site density from intrinsic catalytic activity, we analyzed the ECSA-normalized current densities and estimated the turnover frequencies (TOF) (Fig. S19 and S20). The Cu_2O/Co_xO@NF heterostructure exhibits the highest normalized activity and TOF among the tested samples, demonstrating that its performance enhancement originates from improved intrinsic activity rather than from geometric factors alone. This observation is consistent with recent reports on heterostructured catalysts, where interfacial engineering enhances intrinsic activity by modulating the local electronic structure.[47–49] In our system, this improvement is attributed to the BIEF, which tunes the adsorption energetics of reaction intermediates at each active site, thereby increasing the turnover efficiency and overall catalytic performance. Electrochemical impedance spectroscopy (EIS) further demonstrates that Cu_2O/Co_xO@NF

has the lowest charge-transfer resistance (R_{ct}) of all tested catalysts (Fig. S15), confirming its superior electrical conductivity and rapid interfacial charge-transfer kinetics, consistent with its outstanding OER activity. The decreased charge-transfer resistance (R_{ct}) indicates a reduced interfacial charge-migration barrier, consistent with electric-field-assisted charge transport across the heterojunction. *In situ* EIS was conducted to monitor the evolution of electrocatalytic kinetics and the electrode/electrolyte interface during the OER at different applied potentials. The corresponding Bode phase plots for Cu_2O/Co_xO@NF, Co_xO@NF, and Cu_2O@NF are shown in Fig. 4e and Fig. S9. In these spectra, the low-frequency region (10^{-2}–10^{1} Hz) is associated with a non-uniform charge distribution caused by reactant adsorption, while the high-frequency region (10^{2}–10^{5} Hz) corresponds to oxidation processes within the electrode.[50] As the applied potential increases, phase-angle relaxation decreases and the characteristic frequency shifts toward higher values, indicating accelerated surface reaction rates and reduced faradaic resistance.[11] Notably, the frequency peaks of Cu_2O/Co_xO@NF shift more rapidly to higher frequencies than those of the control catalysts (Fig. 4f), signifying more facile adsorption/desorption of oxygenated intermediates during the OER.[51,52] Collectively, these results demonstrate that the synergistic integration of Co_xO and Cu_2O accelerates electron transfer at the electrolyte–catalyst interface and yields superior OER kinetics. Furthermore, as shown in Fig. 4g and Table S4, the as-synthesized Cu_2O/Co_xO@NF compares favorably with many state-of-the-art OER catalysts reported in the literature, underscoring its potential as a high-performance OER electrocatalyst. Stability is a critical criterion for electrocatalyst evaluation. Long-term durability was assessed *via* chronopotentiometry at 100 mA cm^{-2} for 450 h (Fig. 4h). Cu_2O/Co_xO@NF exhibited excellent stability, maintaining its performance with negligible degradation. Minor potential fluctuations can be attributed to continuous surface reconstruction and bubble release. Post-test SEM analysis after 1000 continuous cyclic voltammetry cycles shows that the catalyst retains its morphology, with only slight agglomeration (Fig. 4h, inset), confirming its structural robustness. Long-term OER testing (400 h at 100 mA cm^{-2}) revealed negligible metal dissolution for the Cu_2O/Co_3O_4@NF catalyst (Table S2). The amount of dissolved Co increased slightly from 6.47×10^{-5} g after 100 h to 9.65×10^{-5} g after 400 h, while dissolved Cu rose from 5.11×10^{-5} g to 8.97×10^{-5} g over the same period. Importantly, the total active-site loss after 400 h remained as low as 2.38%, indicating controlled and slow metal dissolution, as well as excellent structural robustness under prolonged operating conditions.

To distinguish true heterointerfacial synergy from simple additive effects, we prepared a physically mixed Cu_2O/Co_xO (P-Mix) control electrode without an intimate heterojunction. This control sample exhibited a significantly higher overpotential (325 mV *vs.* 298 mV at 100 mA cm^{-2}; Fig. S18), demonstrating that the performance enhancement originates from the engineered heterointerface and its associated built-in electric field, rather than from the mere combination of individual components.

3.3. Unraveling the evolution of dynamic surface reconstruction

Post-OER HR-TEM analysis was conducted to gain deeper insight into the dynamic surface reconstruction of Cu_2O/Co_xO@NF during the OER. As shown in Fig. 5a, the results clearly reveal the *in situ* formation of crystalline CoOOH, with a *d*-spacing of 0.242 nm corresponding to the (101) plane—widely recognized as the actual active phase in cobalt-based OER catalysts.[53] To further elucidate the reconstruction mechanism, *in situ* Raman spectroscopy and mapping were performed on both Cu_2O/Co_xO@NF and Co_xO@NF, ranging from the open-circuit potential (OCP) to 1.55 V (*vs.* RHE) in 0.1 V increments. As shown in Fig. 5d and e, both catalysts eventually develop two characteristic Raman peaks at 475 and 554 cm^{-1}, assigned to the E_g and A_{1g} vibrational modes of CoOOH, respectively,[54–56] providing direct evidence of surface reconstruction during electrolysis. Notably, these CoOOH signatures appear at a lower potential for Cu_2O/Co_xO@NF (1.40 V) than for Co_xO@NF (1.45 V), indicating that Cu_2O incorporation facilitates earlier and more efficient electrochemical reconstruction of the Co_xO phase. To uncover the origin of the enhanced OER performance, *in situ* FTIR spectroscopy was performed on both samples. As shown in Fig. 5g, Cu_2O/Co_xO@NF exhibits a progressively intensifying band at ~1130 cm^{-1} at potentials ≥1.40 V, attributed to the OOH intermediate.[57] In contrast, Co_xO@NF does not show this feature; instead, it displays a band at 1165 cm^{-1} (≥1.45 V, Fig. 5h), corresponding to a superoxo-like OOH species that precedes O_2 release. The detection of OOH-related intermediates on both catalysts confirms an adsorbate evolution mechanism (AEM: OH → O → OOH → O_2).[58,59] Importantly, the *OOH band on Cu_2O/Co_xO@NF is significantly more intense than that on Co_xO@NF, indicating faster oxygen-exchange kinetics. This conclusion is further supported by the pronounced detection of *OH species at ~3350 cm^{-1} on Cu_2O/Co_xO@NF. To identify the active phase generated during OER operation, *ex situ* XRD analysis was performed on the post-test Cu_2O/Co_xO@NF catalyst. The resulting diffraction pattern (Fig. S21) exhibits characteristic reflections corresponding to CoOOH, confirming the *in situ* transformation of the surface into (oxy) hydroxide species that serve as the active sites. This observation is fully consistent with our *in situ* Raman and FTIR results and provides direct experimental evidence supporting the proposed surface-reconstruction mechanism under OER conditions.

The reconstruction process is further corroborated by comparative XPS analysis performed before and after long-term stability testing. The results reveal synchronous increases in the oxidation states of both metal components: the Co^{3+}/Co^{2+} ratio increases from 0.98 to 1.31 (Fig. 5b and i). In contrast, the Cu^{2+}/Cu^{+} ratio shows a substantial increase from 0.17 to 2.09 (Fig. 5c and i). These changes provide direct evidence for the formation of high-valent cobalt and copper species during electrocatalysis. The oxidation of cobalt suggests the generation of a CoOOH-like active phase.[10,60] In contrast, the pro-

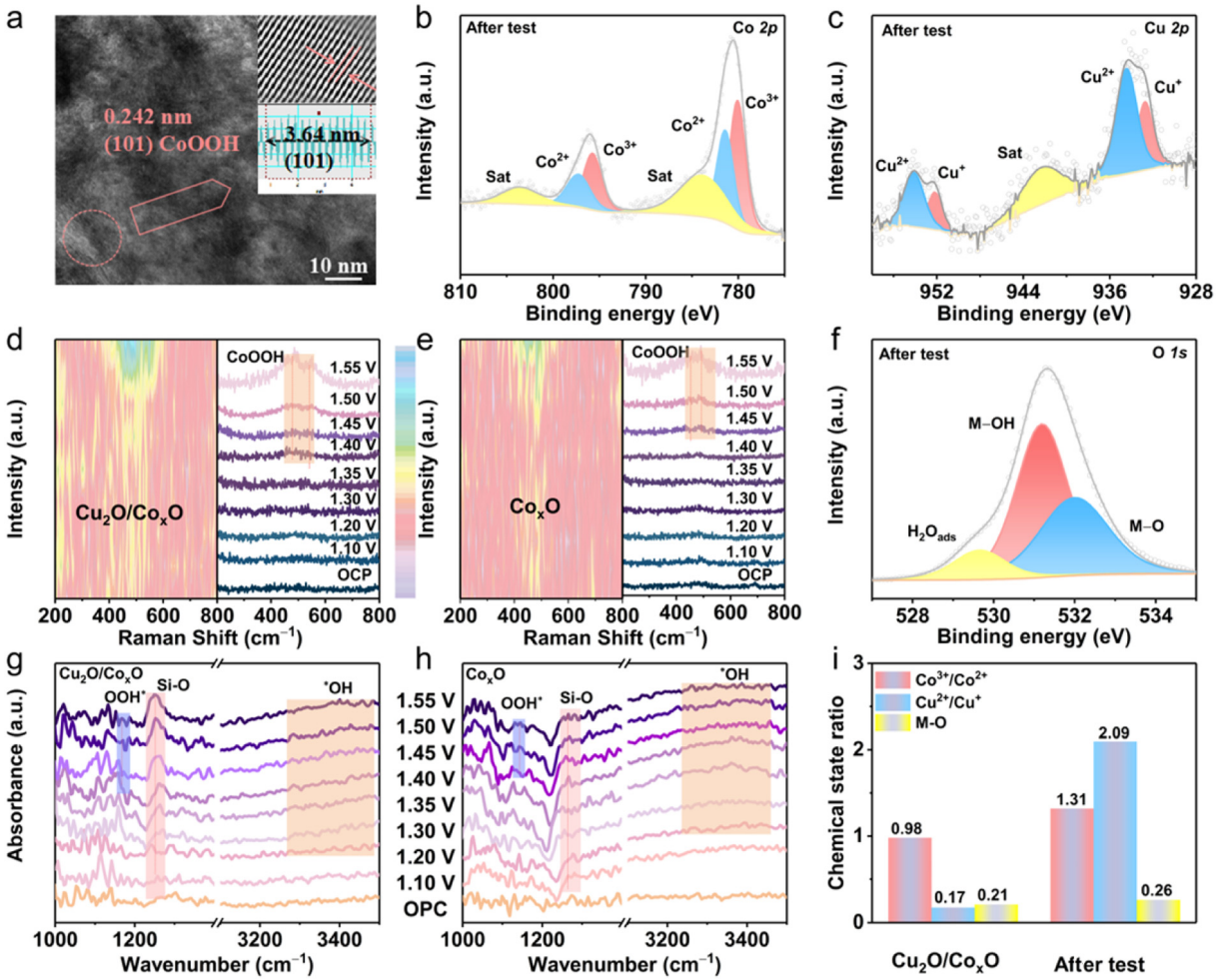

Fig. 5 (a) HRTEM image of Cu_2O/Co_xO@NF after the OER test. XPS analysis of Cu_2O/Co_xO@NF after OER operation at 100 mA cm^{-2}: (b) Co 2p, (c) Cu 2p, and (f) O 1s core-level spectra. (i) Quantitative comparison of the surface molar ratios (Co^{3+}/Co^{2+}, Cu^{2+}/Cu^{+}, and M–O) before and after the stability test, derived from XPS data. *In situ*/*operando* spectroscopic characterization during the OER (all potentials *vs.* RHE). (d and e) *In situ* Raman spectra and intensity mappings for (d) Cu_2O/Co_xO@NF and (e) Co_xO@NF. (g and h) *Operando* ATR-FTIR spectra for (g) Cu_2O/Co_xO@NF and (h) Co_xO@NF.

nounced valence elevation of copper indicates the development of a Cu^{2+}-rich surface layer, a key precursor to catalytically active Cu^{3+} species. This synergistic increase in metal valence states demonstrates that Cu incorporation promotes extensive surface restructuring through electronic modulation, facilitating the formation of abundant, highly active sites responsible for the enhanced OER performance. Further evidence of surface reconstruction is provided by the O 1s spectrum of Cu_2O/Co_xO@NF (Fig. 5f and i), which exhibits characteristic peaks corresponding to M–O and M–OH bonds—associated with CoOOH and CuOOH—as well as adsorbed water (H–OH).[61,62] The increased M–O contribution after the OER confirms the development of a stable, oxygen-rich surface layer. This reconfigured surface is identified as a crucial factor underlying the catalyst's enhanced oxygen-evolution performance and its superior long-term stability.

Post-OER EPR analysis (Fig. S22) confirms the structural persistence of Cu vacancies (g = 2.20), while quantitative XPS results (Fig. 5i) show a pronounced increase in surface Cu^{2+} species accompanied by a corresponding decrease in Cu^{+}. This distinct evolution supports a synergistic mechanism underlying the sustained catalytic activity: the robust Cu-vacancy framework stabilizes the lattice and localizes oxidative transformation to the surface, thereby preventing bulk structural degradation and active-site loss,[63,64] whereas the dynamic Cu^{+}/Cu^{2+} redox couple at the surface continuously participates in and promotes the OER process.[65] Overall, this defect-engineered architecture simultaneously ensures structural integrity and persistent catalytic functionality, accounting for the exceptional operational stability exceeding 450 h.

Although the *in situ* spectroscopic results confirm the formation of CoOOH and the *OOH intermediate, a definitive distinction between the adsorbate evolution mechanism (AEM) and the lattice oxygen mechanism (LOM) would require isotope-labeling experiments (*e.g.*, using $H_2{}^{18}O$). Nevertheless, multiple lines of evidence strongly support a predominantly

AEM pathway: (i) the detection of *OOH, which is a hallmark intermediate of the AEM route, and (ii) the absence of lattice oxygen loss or structural degradation after more than 450 h of OER operation, as confirmed by post-reaction XRD and XPS analyses—behavior inconsistent with the structural instability typically associated with LOM-dominated systems. These observations, together with established literature on Co-based OER catalysts,[66–68] indicate that oxygen evolution on Cu_2O/Co_xO proceeds primarily *via* the AEM pathway. Isotope-labeling studies are planned as future work to provide definitive mechanistic verification.

3.4. Overall water splitting

To evaluate the OER performance of Cu_2O/Co_xO@NF under industrially relevant conditions, a two-electrode electrolyzer was assembled using Cu_2O/Co_xO@NF as the anode and Pt/C@NF as the cathode (Fig. 6a). The polarization curves (Fig. 6b) demonstrate that the $Cu_2O/Co_xO@NF^{(+)}||Pt/C@NF^{(-)}$ electrolyzer delivers markedly superior overall water-splitting performance compared with the $RuO_2@NF^{(+)}||Pt/C@NF^{(-)}$ benchmark, especially at high current densities. Specifically, the electrolyzer requires only 1.77, 1.86, 1.94, and 2.01 V to reach current densities of 100, 200, 300, and 400 mA cm^{-2}, respectively (inset, Fig. 6b). These voltages are significantly lower than those needed for the commercial benchmark under identical testing conditions (1 M KOH, 25 °C). The faradaic efficiency (FE) of Cu_2O/Co_xO@NF for the OER was quantified in 1.0 M KOH using a rotating ring-disk electrode (RRDE). With a disk current (I_D) of 0.518 mA driving the OER, a corresponding ring current (I_R) of 0.189 mA was detected. The calculated FE was 98.57% (Fig. 6c and Fig. S23), confirming excellent catalytic selectivity toward O_2 formation with minimal oxidative by-products. A comparative analysis (Fig. 6d and Table S5) further highlights the superior activity of Cu_2O/Co_xO@NF relative to numerous self-supported electrocatalysts reported for alkaline overall water splitting, particularly at industrially relevant current densities such as 100 mA cm^{-2}.

The $Cu_2O/Co_xO@NF^{(+)}||Pt/C@NF^{(-)}$ electrolyzer also demonstrated outstanding durability. During continuous operation at 100 mA cm^{-2}, the cell voltage remained stable at ~1.77 V for 560 h with virtually no degradation (Fig. 6e), far surpassing the durability of the $RuO_2@NF^{(+)}||Pt/C@NF^{(-)}$ benchmark. Such exceptional stability underscores the structural robustness and long-term reliability of the Cu_2O/Co_xO@NF catalyst. Electrocatalytic hydrogen generation from renewable energy sources under ambient conditions offers a sustainable, decentralized alternative to grid-dependent hydrogen production.[69] This capability was demonstrated by powering the $Cu_2O/Co_xO@NF^{(+)}||Pt/C@NF^{(-)}$ electrolyzer directly with a wind-driven battery and a solar cell. In both cases, efficient water

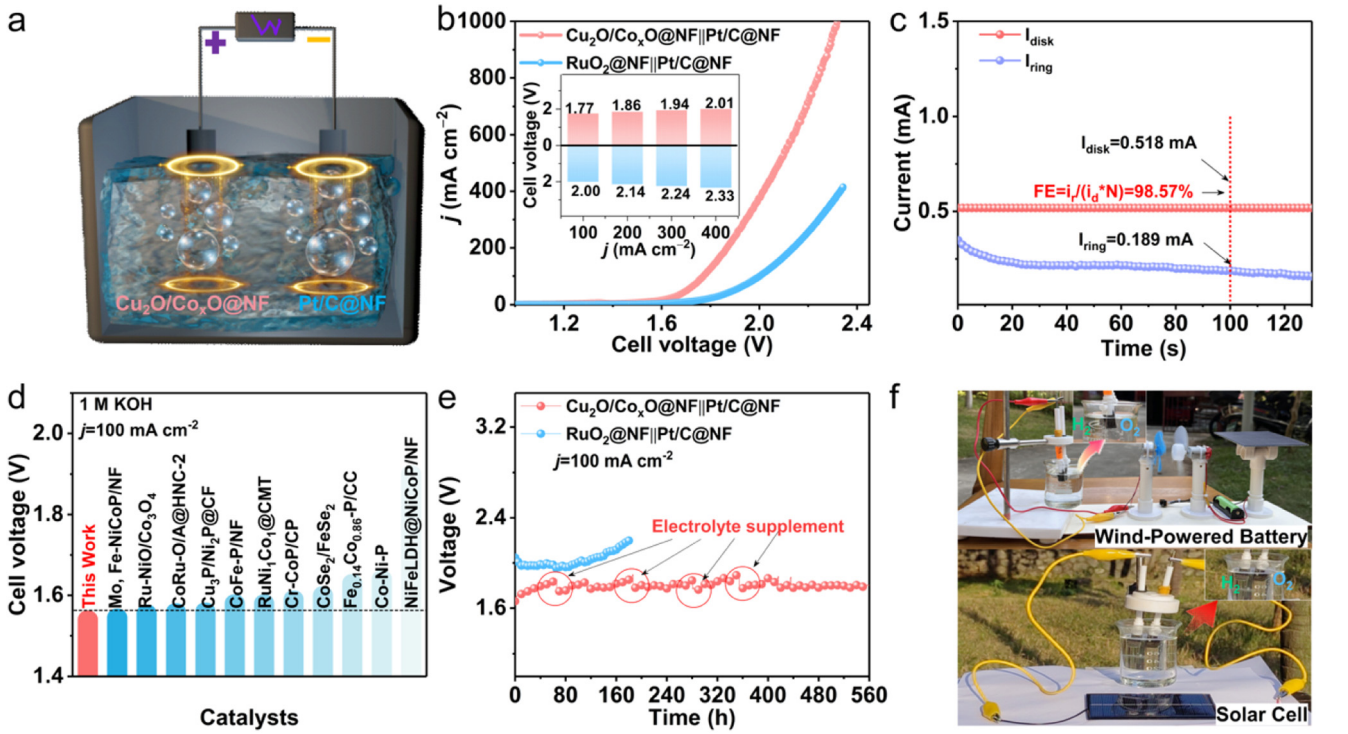

Fig. 6 (a) Experimental setup for overall water splitting in a two-electrode configuration. (b) LSV curves of $Cu_2O/Co_xO@NF^{(+)}||Pt/C@NF^{(-)}$ and the benchmark $RuO_2@NF^{(+)}||Pt/C@NF^{(-)}$ in 1.0 M KOH. All potentials are *iR*-corrected. The inset shows the comparison of the operating voltages at various current densities. (c) Faradaic efficiency of Cu_2O/Co_xO@NF measured by RRDE (1600 rpm) in 1.0 M KOH at a ring potential of 0.4 V *vs.* RHE. (d) Comparison of the cell voltage at 100 mA cm^{-2} for Cu_2O/Co_xO@NF with those reported in the literature. (e) Long-term stability at 100 mA cm^{-2}: $Cu_2O/Co_xO@NF^{(+)}||Pt/C@NF^{(-)}$ *versus* $RuO_2@NF^{(+)}||Pt/C@NF^{(-)}$. (f) Operational diagram of the water-splitting system powered by renewable energy sources (solar- and wind-powered batteries).

splitting was achieved at low voltage (Fig. 6f), and the continuous release of gas bubbles provided explicit visual confirmation of robust operation. These results highlight the strong potential of the Cu_2O/Co_xO@NF anode for off-grid, renewable-energy-driven hydrogen production. The exceptional performance of the Cu_2O/Co_xO@NF electrode arises from a synergistic combination of structural and electronic advantages. Structurally, the 3D binder-free nickel foam substrate provides high conductivity and mechanical stability, significantly increasing the electroactive surface area, reducing interfacial resistance, and facilitating both charge and mass transport. The hierarchical nanoflower morphology further increases the density of active sites, enhances electrolyte diffusion, and enables efficient release of gas bubbles. In addition, the superhydrophilic surface ensures excellent electrolyte wettability, which is essential for stable operation at high current densities.

Electronically, the work-function difference between Co_xO and Cu_2O creates a BIEF at the heterointerface, driving interfacial charge redistribution and accelerating reaction kinetics. The presence of Cu defects provides multiple key benefits: they generate additional active sites, modulate the local electronic structure to optimize intermediate adsorption energies, and serve as triggers to promote dynamic reconstruction of the catalyst surface into the true active (oxy)hydroxide phase during operation. Collectively, this integrated structural—electronic strategy yields a catalyst with exceptional activity, durability, and operational efficiency, making Cu_2O/Co_xO@NF a highly promising candidate for practical alkaline water electrolysis.

4. Conclusion

In this work, we demonstrate that the heterostructured Cu_2O/Co_xO@NF electrocatalyst achieves a synergistic enhancement of catalytic activity and durability by integrating hierarchical nanostructuring, electronic modulation, defect engineering, and dynamic surface reconstruction. The nanoflower morphology increases the accessible active surface area (C_{dl} = 296.2 mF cm^{-2}) and improves mass transport, while abundant Cu vacancy defects and the Cu_2O-Co_xO BIEF significantly accelerate charge transfer and *OH/*OOH adsorption. *In situ* Raman, FTIR, and post-OER XPS collectively reveal rapid electrochemical reconstruction into highly active CoOOH and CuOOH layers, with earlier onset potentials and higher valence-state transitions (Co^{3+}/Co^{2+}: 0.98 → 1.31; Cu^{2+}/Cu^{+}: 0.17 → 2.09). These combined structural and electronic advantages enable Cu_2O/Co_xO@NF to deliver an overpotential as low as 298 mV at 100 mA cm^{-2} and to operate stably for 450 h, outperforming both the Co_xO and Cu_2O counterparts as well as commercial RuO_2. In a practical two-electrode configuration, the catalyst achieves industrially relevant current densities at cell voltages as low as 1.77 V (100 mA cm^{-2}) and demonstrates stable operation for 560 h. The ability to drive water splitting using solar and wind energy further underscores its application potential for decentralized green hydrogen production. Collectively, these results establish Cu_2O/Co_xO@NF as a robust, high-performance OER electrocatalyst and highlight the effectiveness of combining defect engineering, electronic modulation, and dynamic reconstruction to design next-generation catalytic materials for alkaline electrolysis. Aligned with the core principles of Green Chemistry, the Cu_2O/Co_xO@NF catalyst delivers sustainable performance through energy-efficient operation, the use of Earth-abundant Co and Cu, and outstanding long-term stability. Its demonstrated operation at industrially relevant current densities further indicates the potential for reduced capital investment and lower operational costs. A simplified *E*-factor analysis (Table S6) provides an initial quantitative benchmark of the environmental footprint associated with the synthesis process. Although a comprehensive life-cycle assessment and detailed toxicological evaluation would be valuable to fully quantify the overall environmental impact, the current design and performance already establish a solid foundation for the development of practical, scalable, and sustainable electrocatalysts.

Author contributions

Tingting Tang: writing – original draft, data curation, and conceptualization. Zhendong Gao: methodology and data curation. Kuoteng Sun: investigation. Chenggong Niu: formal analysis. Chenxi Shang: investigation. Jingya Guo: writing – review & editing. Jianniao Tian: writing – review & editing. Tayirjan Taylor Isimjan: writing – review & editing. Xiulin Yang: writing – review & editing, supervision, and funding acquisition.

Conflicts of interest

There are no conflicts to declare.

Data availability

Data for this article are available as the supplementary information (SI). Supplementary information: electrochemical data, compound characterization, and experimental data. See DOI: https://doi.org/10.1039/d5gc06935a.

Acknowledgements

This work has been supported by the Guangxi Science and Technology Projects (GUIKE LT2600640010 and GUIKE AD23023004), the National Natural Science Foundation of China (no. 52363028 and 21965005), and the Natural Science Foundation of Guangxi Province (2021GXNSFAA076001).

References

1 S. Zhang, C. Tan, R. Yan, X. Zou, F.-L. Hu, Y. Mi, C. Yan and S. Zhao, *Angew. Chem., Int. Ed.*, 2023, **62**, e202302795.
2 Z.-Y. Wu, F.-Y. Chen, B. Li, S.-W. Yu, Y. Z. Finfrock, D. M. Meira, Q.-Q. Yan, P. Zhu, M.-X. Chen, T.-W. Song, Z. Yin, H.-W. Liang, S. Zhang, G. Wang and H. Wang, *Nat. Mater.*, 2023, **22**, 100–108.
3 D. Wu, Y. Wei, X. Ren, X. Ji, Y. Liu, X. Guo, Z. Liu, A. M. Asiri, Q. Wei and X. Sun, *Adv. Mater.*, 2018, **30**, 1705366.
4 Y. Li, H. Wang, C. Priest, S. Li, P. Xu and G. Wu, *Adv. Mater.*, 2021, **33**, 2000381.
5 H. Li, Y. Zhang, Y. Chen, Y. Li, Z. Li, B. Yang, Q. Zhang, J. Lu, L. Lei, Z. J. Xu and Y. Hou, *Angew. Chem., Int. Ed.*, 2025, **64**, e202423071.
6 Z. Yin, J. Liang, Z. Zhang, H. Luo and J. Zhou, *J. Colloid Interface Sci.*, 2022, **623**, 405–416.
7 W.-K. Chong, B.-J. Ng, Y. J. Lee, L.-L. Tan, L. K. Putri, J. Low, A. R. Mohamed and S.-P. Chai, *Nat. Commun.*, 2023, **14**, 7676.
8 H.-Y. Chen, L. Yang, R.-X. Wang, W.-J. Zhang, R. Liu, Y.-Z. Yun, N. Wang, S. Ramakrishna, L. Jiao and Y.-Z. Long, *Small*, 2023, **19**, 2304086.
9 W. Zhang, L. Yang, Z. Li, G. Nie, X. Cao, Z. Fang, X. Wang, S. Ramakrishna, Y. Long and L. Jiao, *Angew. Chem., Int. Ed.*, 2024, **63**, e202400888.
10 C. Jia, Y. Chen, C. Zhou, X. Xiang, X. Long, B. Zhao, N. Zhang, S. Zhao, L. Chai, X. Liu and Z. Lin, *ACS Nano*, 2025, **19**, 19938–19950.
11 Z. Xiao, Y.-C. Huang, C.-L. Dong, C. Xie, Z. Liu, S. Du, W. Chen, D. Yan, L. Tao, Z. Shu, G. Zhang, H. Duan, Y. Wang, Y. Zou, R. Chen and S. Wang, *J. Am. Chem. Soc.*, 2020, **142**, 12087–12095.
12 L. Xu, Q. Jiang, Z. Xiao, X. Li, J. Huo, S. Wang and L. Dai, *Angew. Chem., Int. Ed.*, 2016, **55**, 5277–5281.
13 X. Zhang, X. Zhao, B. Bateer, Y. Jiao, A. Wu, H. Yan, D. Wang, J. Wang and C. Tian, *J. Mater. Chem. A*, 2025, **13**, 7274–7283.
14 T. Tang, Y. Teng, K. Sun, F. Wei, L. Shi, Y. Chen, S. Muhammad, T. T. Isimjan, J. Tian and X. Yang, *ChemSusChem*, 2025, **18**, e202401872.
15 M. Assis, A. C. M. Rennó, J. Andrés and E. Longo, *ACS Omega*, 2025, **10**, 22323–22346.
16 Z.-K. Han, W. Liu and Y. Gao, *JACS Au*, 2025, **5**, 1549–1569.
17 G. Zhuang, Y. Chen, Z. Zhuang, Y. Yu and J. Yu, *Sci. China Mater.*, 2020, **63**, 2089–2118.
18 X. Yan, X. Han and J. He, *J. Phys. Chem. Lett.*, 2025, **16**, 4428–4435.
19 D. Chen, R. Lu, R. Yu, Y. Dai, H. Zhao, D. Wu, P. Wang, J. Zhu, Z. Pu, L. Chen, J. Yu and S. Mu, *Angew. Chem., Int. Ed.*, 2022, **61**, e202208642.
20 H. Zhao, D. Chen, Y. Dong, Y. Chen, J. Jiao, J. Yu, Y. Li and S. Mu, *Appl. Catal., B*, 2025, **374**, 125409.
21 X. Mu, Y. Yuan, M. Yu, Y. Hu, W. Zeng, W. Peng, Y. Zhang, X. Liu, S. Liu and S. Mu, *Nano Energy*, 2024, **131**, 110216.
22 Y. Sun, Y. Li, S. You, X. Li, Y. Zhang, Z. Cai, M. Liu, N. Ren and J. Zou, *Chem. Eng. J.*, 2021, **424**, 130460.
23 M. Li, J. Sun, X. Zhou, H. Yao, B. Cong, Y. Li and G. Chen, *Appl. Catal., B*, 2023, **322**, 122096.
24 Z. Wang, L. Zhang, T. U. Schülli, Y. Bai, S. A. Monny, A. Du and L. Wang, *Angew. Chem., Int. Ed.*, 2019, **58**, 17604–17609.
25 F. Wang and J. He, *Adv. Mater.*, 2020, **370**, 525–526.
26 S. Zhao, Y. Wang, Y. Hao, L. Yin, C.-H. Kuo, H.-Y. Chen, L. Li and S. Peng, *Adv. Mater.*, 2024, **36**, 2308925.
27 P. Zhou, X. Lv, S. Tao, J. Wu, H. Wang, X. Wei, T. Wang, B. Zhou, Y. Lu, T. Frauenheim, X. Fu, S. Wang and Y. Zou, *Adv. Mater.*, 2022, **34**, 2204089.
28 M. Liu, Z. Sun, S. Li, X. Nie, Y. Liu, E. Wang and Z. Zhao, *J. Mater. Chem. A*, 2021, **9**, 22129–22139.
29 Q. Zhang, W. Zhang, J. Zhu, X. Zhou, G.-R. Xu, D. Chen, Z. Wu and L. Wang, *Adv. Energy Mater.*, 2024, **14**, 2304546.
30 Y. Sun, R. Li, X. Chen, J. Wu, Y. Xie, X. Wang, K. Ma, L. Wang, Z. Zhang, Q. Liao, Z. Kang and Y. Zhang, *Adv. Energy Mater.*, 2021, **11**, 2003755.
31 J. Li, J. Li, J. Ren, H. Hong, D. Liu, L. Liu and D. Wang, *Nano-Micro Lett.*, 2022, **14**, 148.
32 X. Chen, X. Xu, C. Shao, Z. Ke, Y. Cheng, H. Jin, Y. Da, D. Liu and W. Chen, *ACS Energy Lett.*, 2024, **9**, 2182–2192.
33 X. Yang, Z. Zhou, Y. Zou, J. Kuang, D. Ye, S. Zhang, Q. Gao, S. Yang, X. Cai and Y. Fang, *Appl. Catal., B*, 2023, **325**, 122332.
34 H. Cheng, M.-L. Li, C.-Y. Su, N. Li and Z.-Q. Liu, *Adv. Funct. Mater.*, 2017, **27**, 1701833.
35 H. A. Bandal and H. Kim, *Appl. Surf. Sci.*, 2023, **622**, 156925.
36 X. Zhao, F. Li, R. Wang, J.-M. Seo, H.-J. Choi, S.-M. Jung, J. Mahmood, I.-Y. Jeon and J.-B. Baek, *Adv. Funct. Mater.*, 2017, **27**, 1605717.
37 J. Balamurugan, T. T. Nguyen, N. H. Kim, D. H. Kim and J. H. Lee, *Nano Energy*, 2021, **85**, 105987.
38 L. Zhang, Y. Zhu, Z. Nie, Z. Li, Y. Ye, L. Li, J. Hong, Z. Bi, Y. Zhou and G. Hu, *ACS Nano*, 2021, **15**, 13399–13414.
39 X. Li, P. Wang, M. Niu, W. Cui, Y. Wan, J. Zhang, J. Zheng and Y.-Z. Long, *Appl. Surf. Sci.*, 2025, **690**, 162626.
40 C. Feng, W. Zhou, H. Wu, Q. Huo, J. Shao, X. Li, H. Yang, Q. Hu and C. He, *Appl. Catal., B*, 2024, **341**, 123280.
41 Z. Huang, D. Zhang, Z. Chen and S. Xia, *J. Environ. Chem. Eng.*, 2025, **13**, 119025.
42 J. Cai, X. Zhang, Y. Shi, Y. Ye and S. Lin, *ACS Sustainable Chem. Eng.*, 2022, **10**, 5986–5997.
43 W. Zheng, *ACS Energy Lett.*, 2023, **8**, 1952–1958.
44 S. Sun, G. Sun, P. Cheng, R. Liu and C. Zhang, *Mater. Today Energy*, 2023, **32**, 101246.
45 J. Fan, J. Xia, H. Wang, H. Li, Y. Tao, G. Wang, W. Hao, Q. Bi, G. Li, X. Shen and L. Ai, *Adv. Energy Mater.*, 2025, **15**, 2501995.
46 H. Liu, R. Xie, Y. Luo, Z. Cui, Q. Yu, Z. Gao, Z. Zhang, F. Yang, X. Kang, S. Ge, S. Li, X. Gao, G. Chai, L. Liu and B. Liu, *Nat. Commun.*, 2022, **13**, 6382.

47 L. Wei, J. Dai, S. Qin, M. Wang, Z. Zhu, W. Xu, K. Liu and J. Wan, *Green Chem.*, 2025, **27**, 8755–8776.
48 J. a. Dai, J. Xian, K. Liu, Z. Wu, M. Fan, S. Qin, H. Jiang, W. Xu, H. Jin and J. Wan, *Chin. J. Catal.*, 2025, **74**, 228–239.
49 Z. Wu, M. Fan, H. Jiang, J. Dai, K. Liu, R. Hu, S. Qin, W. Xu, Y. Yao and J. Wan, *Angew. Chem., Int. Ed.*, 2025, **64**, e202413932.
50 H. Jia, N. Yao, Y. Jin, L. Wu, J. Zhu and W. Luo, *Nat. Commun.*, 2024, **15**, 5419.
51 F. Wei, Q. Peng, T. Sun, J. Zhu, Z. Luo, D. Wang, X. Yang, S. Sun and B. Wu, *Nano Energy*, 2025, **139**, 110961.
52 Y. Zhang, Z. Li, H. Jang, M. G. Kim, J. Cho, S. Liu, X. Liu and Q. Qin, *Adv. Mater.*, 2025, **37**, 2501586.
53 T. Tang, Y. Chen, K. Sun, Y. Teng, F. Wei, T. T. Isimjan, J. Guo, J. Tian and X. Yang, *J. Colloid Interface Sci.*, 2025, **690**, 137314.
54 B. Sun, S. Zhang, H. Yang, T. Zhang, Q. Dong, W. Zhang, J. Ding, X. Liu, L. Wang, X. Han and W. Hu, *Adv. Funct. Mater.*, 2024, **34**, 2315862.
55 L. Guo, J. Chi, T. Cui, J. Zhu, Y. Xia, H. Guo, J. Lai and L. Wang, *Adv. Energy Mater.*, 2024, **14**, 2400975.
56 S. Min, G. Yang, Y. Jiao, J. Wang, Y. Liu, Z. Chen, H. Yan and H. Fu, *Adv. Funct. Mater.*, 2026, **36**, e14250.
57 P.-C. Yu, X.-L. Zhang, T.-Y. Zhang, X.-Y.-N. Tao, Y. Yang, Y.-H. Wang, S.-C. Zhang, F.-Y. Gao, Z.-Z. Niu, M.-H. Fan and M.-R. Gao, *J. Am. Chem. Soc.*, 2024, **146**, 20379–20390.
58 M. Zhang, M. de Respinis and H. Frei, *Nat. Chem.*, 2014, **6**, 362–367.
59 J. Chang, Y. Shi, H. Wu, J. Yu, W. Jing, S. Wang, G. I. N. Waterhouse, Z. Tang and S. Lu, *J. Am. Chem. Soc.*, 2024, **146**, 12958–12968.
60 N. Zhang and Y. Chai, *Energy Environ. Sci.*, 2021, **14**, 4647–4671.
61 F. Chen, C. Shen, Y. Zhu, Y. Liu, D. Zhou, L. Huang, L. Shi, H. Zhang, S. Cao and R. Jia, *Appl. Surf. Sci.*, 2024, **653**, 159357.
62 X. Chen, Q. Wang, Y. Cheng, H. Xing, J. Li, X. Zhu, L. Ma, Y. Li and D. Liu, *Adv. Funct. Mater.*, 2022, **32**, 2112674.
63 B. C. Wyatt, M. G. Boebinger, Z. D. Hood, S. Adhikari, P. P. Michałowski, S. K. Nemani, M. G. Muraleedharan, A. Bedford, W. J. Highland, P. R. C. Kent, R. R. Unocic and B. Anasori, *Nat. Commun.*, 2024, **15**, 6353.
64 N. Zhou, J. Wang, N. Zhang, Z. Wang, H. Wang, G. Huang, D. Bao, H. Zhong and X. Zhang, *Chin. J. Catal.*, 2023, **50**, 324–333.
65 Z. Zhang, Z.-L. Wang, K. An, J. Wang, S. Zhang, P. Song, Y. Bando, Y. Yamauchi and Y. Liu, *Small*, 2021, **17**, 2008052.
66 X. Dong, H. Huang, L. Huang, Y. Zhou, B. Zhang, H. Zeng, Z. Lin and G. Zou, *Angew. Chem., Int. Ed.*, 2024, **63**, e202318976.
67 J. Wang, Y. Gao, H. Kong, J. Kim, S. Choi, F. Ciucci, Y. Hao, S. Yang, Z. Shao and J. Lim, *Chem. Soc. Rev.*, 2020, **49**, 9154–9196.
68 B. Zhang, X. Zheng, O. Voznyy, R. Comin, M. Bajdich, M. García-Melchor, L. Han, J. Xu, M. Liu, L. Zheng, F. P. García de Arquer, C. T. Dinh, F. Fan, M. Yuan, E. Yassitepe, N. Chen, T. Regier, P. Liu, Y. Li, P. De Luna, A. Janmohamed, H. L. Xin, H. Yang, A. Vojvodic and E. H. Sargent, *Science*, 2016, **352**, 333–337.
69 D. Chen, H. Bai, J. Zhu, C. Wu, H. Zhao, D. Wu, J. Jiao, P. Ji and S. Mu, *Adv. Energy Mater.*, 2023, **13**, 2300499.

